Acta Materialia 293 (2025) 121095

Contents lists available at ScienceDirect

Acta Materialia

journal homepage: www.elsevier.com/locate/actamat

Full length article

Intermetallic dispersion-strengthened ferritic superalloys with exceptional resistance to radiation-induced hardening

Kan Ma [a,j,*], Pedro A. Ferreirós [a,k], Thomas W. Pfeifer [b], Robert G. Abernethy [c], Sophia von Tiedemann [a], Nianhua Peng [d], Graeme Greaves [e], Colin Ophus [f,g], Kai Sun [h], Anamul H Mir [e], Lumin Wang [i], Shasha Huang [j], Shijun Zhao [j], Patrick E. Hopkins [b], Christopher D. Hardie [c], Alexander J. Knowles [a,c,*]

[a] School of Metallurgy and Materials, University of Birmingham, Birmingham B15 2TT, United Kingdom
[b] Department of Materials Science and Engineering, University of Virginia, Charlottesville, VA 22904, USA
[c] UK Atomic Energy Authority, Culham Science Centre, Abingdon, OX14 3DB, United Kingdom
[d] Surrey Ion Beam Centre, Surrey University, Guildford GU2 7XH, United Kingdom
[e] MIAMI Irradiation Facility, School of Computing and Engineering, University of Huddersfield, HD1 3DH, UK
[f] Department of Materials Science and Engineering, Stanford University, Stanford, CA 94305, USA
[g] Precourt Institute for Energy, Stanford University, Stanford, 94305, USA
[h] Department of Materials Science and Engineering, University of Michigan, Ann Arbor, MI48109, USA
[i] Department of Nuclear Engineering and Radiological Sciences, University of Michigan, Ann Arbor, MI, 48109, USA
[j] Department of Mechanical Engineering, City University of Hong Kong, Hong Kong, China
[k] Advanced Materials for Nuclear Energy, VTT Technical Research Centre of Finland, 02150 Espoo, Finland

ARTICLE INFO

Keywords:
Intermetallic dispersion-strengthening
Interface
Radiation-induced hardening
Dislocation
Disordering

ABSTRACT

Intermetallic dispersion-strengthening (IDS) using nano-scale coherent intermetallic precipitates offers a potent strategy to produce high-strength and radiation-resistant steels, whilst addressing the manufacturability challenges of analogous oxide dispersion-strengthened (ODS) steels. However, their performance with intermetallic stability under irradiation damage, such as radiation-induced hardening (RIH), whilst hypothesised, is undemonstrated. Here, we report on a model IDS α(A2) + α'($L2_1$) Fe-Ni-Al-Ti ferritic superalloy, which exhibits exceptional resistance to RIH with near-zero hardening after irradiation at 300 °C 1 dpa, in contrast to significant RIH in a counterpart coarse precipitate alloy (increase in nano-hardness of 1.0 GPa) and Eurofer97 (0.7 GPa). This irradiation resistance is attributed to the high density of semi-coherent precipitate-matrix interfaces, and partial-disordering $L2_1$->B2 which causes a decrease in anti-phase boundary energy. High interface density with localised interfacial strain offers effective sinks, suppressing defect populations compared to the counterpart with lower interface density. Meanwhile, atomic resolution spectroscopy and irradiation with in-situ transmission electron microscopy show that the disordering stems from Al-rich and Ti-rich sublattices mixing in the initial $L2_1$—Ni_2AlTi structure below 500 °C, forming metastable B2-Ni(Al,Ti). Combined, the high interface density and radiation-induced intermetallic disordering underpin the remarkable radiation tolerance, demonstrating the IDS concept as a promising radiation-resistant materials design strategy.

1. Introduction

Structural materials in nuclear reactors undergo irradiation damage, generating excess self-interstitial atoms (SIA) and vacancies. These point defects, on the one hand, modify the microstructure by forming microstructural defects, and, on the other hand, their diffusion changes elemental distributions and phases/voids/bubbles [1–3]. Such changes in microstructure cause degradation of material properties, including an expansion of the physical volume, i.e. void swelling, and an increase in strength along with a decrease in ductility, i.e. radiation-induced hardening (RIH), which threaten the integrity and reliability of the structure [4]. Two general strategies to design radiation-tolerant materials are to utilise radiation-resistant matrix phases, such as body-centred cubic (bcc) structure or high entropy alloy design, and to

* Corresponding authors.
E-mail addresses: kan.ma@cityu.edu.hk (K. Ma), a.j.knowles@bham.ac.uk (A.J. Knowles).

https://doi.org/10.1016/j.actamat.2025.121095
Received 31 December 2024; Received in revised form 21 March 2025; Accepted 29 April 2025
Available online 2 May 2025

increase the defect sinks [5]. Following these strategies, oxide-dispersion-strengthened (ODS) steels were designed to contain a high interface area with nano-oxide particles and a fine-grained ferritic/martensitic matrix [5–9]. Some ODS materials have demonstrated superior void swelling resistance up to a dose of more than 100 dpa [10–12] and reduced RIH compared to non-ODS counterparts [13,14]. However, challenges remain concerning their manufacturability and joining methods at commercial scales [15,16]. The development of alternative radiation-tolerant materials is still in demand for advancing fission and fusion technologies.

In the last decade, there has been rapid development of advanced steels reinforced by dispersed intermetallics, whereby the initiative was to introduce ordered intermetallic precipitates for improved mechanical properties at high temperatures such as creep resistance [17–21], inspired by the γ-γ' microstructure of Ni superalloys. Such a new class of materials known as ferritic superalloys have been designed driven by CALPHAD methods [17,22–24]. They comprise a disordered body-centred cubic (bcc) matrix (α for steel and β for other metals) reinforced by coherent or semi-coherent ordered-bcc intermetallics (β'), such as B2-NiAl [25,26] and Heusler phase $L2_1$—Ni_2AlTi [21,27], as shown in Fig. 1a. Ferritic superalloys not only exhibit exceptional improvements in high-temperature mechanical properties but also present significant advantages in the fabrication process and cost for application compared to ODS steels. Based on ferritic superalloys, ODS-like 'intermetallic dispersion-strengthened' (IDS) steels bearing a high matrix-precipitate interface density for point defect recombination are proposed to withstand radiation environments. Compared to face-centred cubic (fcc) γ-γ' Ni-based superalloys, bcc ferritic alloys offer a low activation and low void swelling matrix. However, the radiation behaviour and the role of the coherent interface in ferritic superalloys and IDS steels need to be explored. Intriguingly, a recent study has demonstrated superior void swelling resistance of B2-Ni(Al,Fe) nanoparticle-strengthened martensitic steel over ODS steels [28]. The phase transformation, including the in-situ dissolution of ordered phase precipitates and the reprecipitation, promoted in-situ defect annealing and efficiently prevented the formation of voids over 500 °C. However, structure and composition of precipitates are susceptible to radiation damage, as shown in other precipitate-strengthened alloys [29,30], which will lead to changes in mechanical properties. The RIH behaviour of IDS-type ferritic alloys remains still unknown.

While ferritic materials exhibit good void swelling resistance at elevated irradiation temperatures (>0.4T_m with T_m the melting temperature in Kelvin), their critical concerns is RIH at lower operating temperatures (0.3–0.4T_m, e.g., ≤500 °C). It is known that irradiation hardening and embrittlement are phenomena that predominantly emerge and evolve at early-stage damage levels (0.001–0.1 dpa) [4]. For

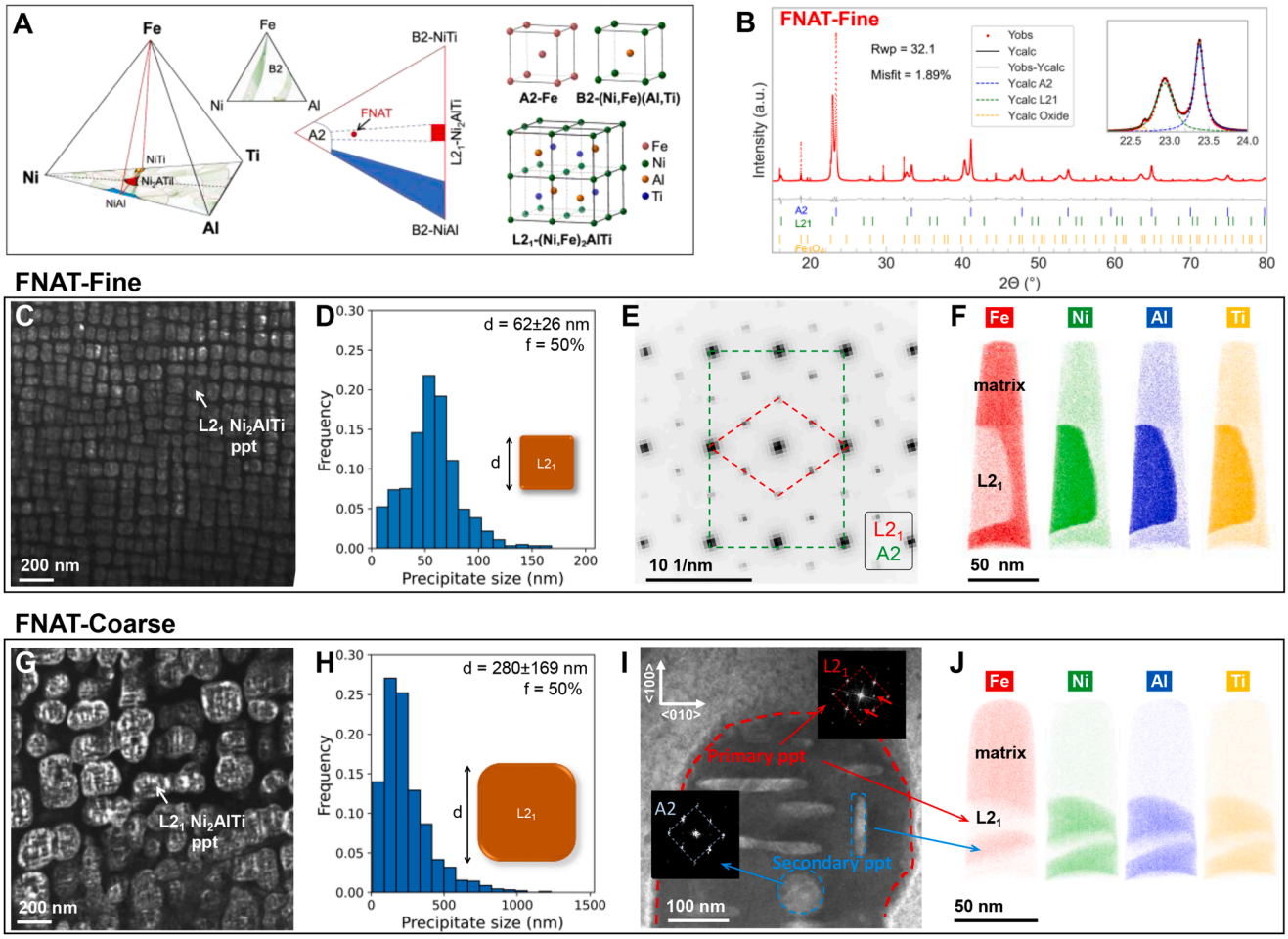

Fig. 1. Design and microstructure of FNAT alloys. (a) Schematic phase diagram of Fe-Ni-Al-Ti systems at 1200 °C calculated using TCNI8 database of ThermoCalc with the unit cell of three bcc phases in ferritic alloy systems. (b) SXRD patterns of FNAT-Fine and FNAT-Coarse showing the A2+$L2_1$ microstructure with the inset enlarged profiles of FNAT-Fine showing the pattern refinement. Microstructure of FNAT-Fine: (c) TEM/DF image using an $L2_1$ reflection, (d) precipitate (ppt) size distribution with d the side length and f the area fraction, (e) TEM SAED patterns along a zone axis ⟨011⟩ with (f) APT element maps showing the microstructure consisting of an A2 Fe-rich matrix and $L2_1$—Ni2AlTi precipitate. Microstructure of FNAT-Coarse: (g) TEM/DF image showing the A2 matrix and $L2_1$ precipitates microstructure; (h) precipitate size distribution; (i) HR-STEM/HAADF image with (j) APT element maps, showing a hierarchical A2-$L2_1$-A2 structure. Secondary A2 Fe-rich precipitates have a disc morphology preferentially growing in {001} planes. Phase composition by APT in (f) and (j) in Table 1.

example, high radiation-induced hardening was revealed in Fe and Fe-Cr alloys at 0.6 dpa between 300–500 °C [31]. For IDS alloys, while their high matrix-precipitate interface density may enhance defect annihilation, the intrinsic phase stability of reinforcing intermetallics (e.g., B2, $L2_1$) and their dynamic response to irradiation—such as disordering or amorphisation—remain unresolved. Specifically, if nanoprecipitates lose coherency or degrade under irradiation, their effectiveness as defect sinks could diminish, exacerbating matrix hardening. Thus, understanding the interplay between precipitate microstructure (e.g., interface density, phase stability) at early-stage of irradiation is critical to designing IDS alloys with balanced swelling resistance and hardening resistance.

Here, we consider Fe-Ni-Al-Ti alloys as the template system of IDS-type ferritic alloys to study RIH behaviour. Fe-Ni-Al-Ti systems offers a wide range of alloys with exceptional mechanical properties. High content of Ni (>30 at.%) promote a fcc matrix with either $L1_2$ ordered-fcc [32] or bcc [33] strengthening phase. However, high Ni content will increase the radio-activity of materials after neutron irradiation and a fcc matrix, as explained above, is less resistant to void swelling than a bcc one. Low content of Ni (<30 at.%) promotes ferritic superalloy with a bcc matrix. Recent advancements demonstrate that carbon-free Fe-Ni-Al-Cr-Ti alloys achieve exceptional creep resistance up to 700 °C, compared to their Ti-free counterparts, via hierarchical B2-NiAl precipitates with $L2_1$—Ni_2TiAl sub-precipitates within a bcc-Fe matrix [17,34,35]. These hierarchically structured phases arise from double miscibility gaps in the Fe-Ni-Al-Ti system [36,37]. Al additions (2.5–10 wt.%, i.e., ~5–19 at.%) stabilise the bcc matrix by inhibiting bcc-to-fcc transformation [38] and could enhance oxidation resistance. As bulk Ni_2AlTi and the two-phase NiAl/Ni_2AlTi alloys exhibit significantly improved creep resistance compared to single-phase NiAl [39,40], Ti (< 5 at.%) is added to replace Al, which modifies the B2 phase into $L2_1$—Ni_2TiAl. This increases lattice misfit between precipitates and the matrix, which strengthens the material by impeding dislocation climb and enhancing creep properties [35]. Recently, different from other FNAT alloys, a high content of Ti (~13.5 at.%) is added into Fe with equal amount of Al to create a novel Fe-Ni_2AlTi alloy [27]. This alloy exhibits microstructure with cuboidal precipitates, similar to Ni-based superalloys CMSX-4. Micromechanical testing with digital image correlation (DIC) reveals that the Fe-Ni_2AlTi alloy minimises plastic strain mismatch at precipitate-matrix interfaces, reducing interfacial stresses (~3 × lower than Ni-based CMSX-4), which enables ductility retention under tensile loading without strength loss, showcasing a critical advantage for high-performance structural applications.

In this work, we present a study of irradiation behaviour of two model Fe-Ni_2AlTi IDS alloys (FNAT for short) with the same composition as [27] to achieve a superalloy-type microstructure: reinforced by (semi-)coherent $L2_1$—Ni_2AlTi intermetallic precipitates. These FNAT alloys along with a standard ferritic-martensitic (FM) steel Eurofer97 were irradiated with heavy ions to study the role of fine precipitates in ferritic superalloys on RIH. The FNAT-Fine alloy with a high sink density within the range of ODS steels shows exceptional resistance to RIH compared to its counterpart alloy FNAT-Coarse with a low sink density within the range of FM steels, revealing the effectiveness of semi-coherent precipitate-matrix interfaces as sinks for point defects in IDS design. Post-irradiation transmission electron microscopy (TEM) characterisation combined with in-situ irradiation experiments aims to evaluate the propensity of the reinforcing intermetallics to disordering or amorphisation under irradiation. Results show that high interface density effectively suppresses the formation of dislocation loops and the $L2_1$-to-B2 disordering under irradiation at temperatures lower than 500 °C offers also an offset of on the RIH. Combining the prevailing mechanisms of interface-enhancing recombination, the new mechanism of in-situ partial disordering from $L2_1$ to B2 in IDS provides a new design perspective for nuclear materials.

2. Materials and methods

2.1. Materials and sample preparation

The as-cast Fe-20Ni-13.5Al-13.5Ti (in at. %) alloy was manufactured by arc melting elements of 99.95% purity. Impurity content was measured as 0.007, 0.003, 0.002, 0.01, 0.16 wt percent for C, S, N, O, Si respectively by a 'LECO Corporation' (www.leco.com) combustion analyse. The sample was turned and remelted five times to ensure chemical homogeneity. Samples were encapsulated in silica glass ampoules backfilled with argon to avoid oxidation. The two FNAT alloys received a heat treatment at 1200 ± 5 °C for 2 h; then were water quenched to room temperature. FNAT-Coarse was again encapsulated and aged at 700 ± 5 °C for 8 hours followed by water quenching. All heat treatments were carried out in a Carbolite CWF1300/5 furnace. The homogenised and aged samples are respectively abbreviated to FNAT-Fine and FNAT-Coarse. In addition, Eurofer97 (Fe-10.2Cr-1.6Al-9.4 W, at.%) with a bcc ferritic matrix was used to conduct a comparative study.

Thin slices (2 mm thick, 20 × 10 mm rectangles) were cut from each material, then mounted, ground and polished using an oxide polishing suspension (OPS) to achieve a mirror-like surface. The microstructure of these samples was characterised by a Field Emission Gun (FEG) Scanning Electron Microscopy (SEM, JEOL 7000F) operating at 20 kV equipped with Oxford INCA energy dispersive X-ray spectroscopy (EDS) detector. The bulk composition of the alloys was evaluated by averaging five 200 × 200 μm area measurements at five regions of the sample. The composition of two FNAT alloys are given in Table S1. The small standard deviation indicates a low macro-segregation. SEM images were analysed using a machine learning plugin tool in ImageJ, trainable Weka segmentation, to obtain the size distribution of the precipitates.

2.2. Synchrotron X-ray diffraction

Synchrotron X-ray diffraction (SXRD) analysis was conducted on powder derived from FNAT-Fine and FNAT-Coarse alloys. The powder was obtained through mechanical grinding of bulk samples. Afterwards, the powder was contained in an alumina crucible and then encapsulated with titanium flakes as oxygen getters under argon, followed by annealing at 500 °C for 15 min. This annealing process aims to relieve stress in the powder. Subsequently, the powder was loaded into borosilicate capillaries with a diameter of 0.5 mm. Control measurements were also carried out on powders without annealing to identify oxide peaks observed in the stress-relieved powder. SXRD experiments were conducted on Beamline I11 at Diamond Light Source. A wide-angle position-sensitive detector with an intrinsic 2θ step size of 4 millidegrees was employed. The wavelength (λ) used was 82.6596(10) pm, calibrated using a NIST Si 640c standard, and the collection time was set at 120 s. Rietveld refinement of the XRD pattern was performed using the FULLPROF Suite. This refinement aimed to determine the lattice parameters of the ferritic A2 matrix and $L2_1$ precipitates. Additionally, the lattice misfit (δ) between the A2 matrix and $L2_1$ precipitates was calculated as follows.

$$\delta = \frac{2(a_{L21} - 2a_{A2})}{a_{L21} + 2a_{A2}}$$

2.3. Irradiation experiments

The irradiation experiment for nano-indentation was performed at the University of Surrey. Thin slices were irradiated by 2 MeV Fe^+ ions at 300 ± 10 °C using a rastered beam. The temperature was monitored by a thermocouple attached to the aluminium stub where samples were attached. The ion flux was 1.5 ± 0.2 × 10^{11} ions cm^{-2} s^{-1} and the fluence was 1.1 ± 0.2 × 10^{15} ions cm^{-2}. The damage profile was calculated by the Stopping Range of Ions in Matter (SRIM) 2013 code using the Kinchin-Pease option with a displacement threshold energy of

40/40/25/30 eV for Fe/Ni/Al/Ti respectively. The dose in dpa was calculated based on the Norgett, Robinson and Torrens (NRT) model using the following equation:

$$dose = \frac{k\left(E_{recoil} - E_{r,ionise}\right)}{2\overline{E_d}} \frac{\phi}{N}$$

where k=0.8 is the displacement efficiency, E_{recoil} is the energy absorbed by target atoms, $E_{r,ionize}$ is the target atom energy lost to ionisation, $\overline{E_d}$=36.6 eV is the weighted average displacement energy using atomic percent of each element and their E_d, ϕ is the ion fluence and N=8.11 × 10^{22} atoms/m^3 is the atom density of the alloy. The damage and implantation profiles were plotted in Fig. S1a.The final dose varied from 0.5 dpa near the surface to 1.2 dpa near the peak damage depth of 600 nm. Before irradiation, shielding was placed at about 1 mm from two parallel edges so that the regions approximately 1 mm wide along these edges were unirradiated. After irradiation, a boundary contrast dividing the irradiated and unirradiated region was evident in secondary electron imaging.

In-situ ion irradiation was performed in two campaigns, (i) using a 300 kV FEI Tecnai G2 F30 TWIN TEM at Michigan Center for Materials Characterisation (MC)^2 at the University of Michigan and (ii) using a 300 kV Hitachi H-9500 TEM at the MIAMI-2 facility at the University of Huddersfield. For (i), TEM lamellae prepared by FIB were mounted on a heating chip and irradiated by 1170 keV Kr^{3+} with an average ion flux of 4.51 × 10^{11} ions cm^2 s^{-1}. The ion incident angle, i.e., the angle between the incoming ion beam and the normal (perpendicular) to the substrate surface, was about 40° The irradiations were carried out at room temperature and 300/400/500 °C. For (ii), TEM lamella was mounted on a copper FIB grid and irradiated by 900 keV Kr^{3+} ions with an average flux of 3.87 × 10^{11} ions cm^2 s^{-1}. The ion incident angle was about 10° The samples were heated by a Gatan heating TEM holder. The irradiations were carried out at room temperature and 150/425/450/500 °C. Considering that TEM samples are thin, the dose rates are calculated by averaging the value between 0–100 nm thickness, which leads to (i) 0.061 dpa/min and (ii) 0.043 dpa min^{-1} (see profiles in Fig. S1(b,c)). Different Kr ion energies are due to the platform capacity. Irradiation at room temperature and 500 °C were repeated at both platforms and showed the same results. In all experiments, the diffraction patterns along the pre-selected zone axis, either <101> or ⟨112⟩ were captured along the irradiation to reveal the disordering of $L2_1$ as a function of dose.

2.4. Nano-indentation

Nanoindentation experiments were carried out in regions within the unirradiated and irradiated zones in each sample between 1500 nm and 2000 μm depth. The measurement was performed at room temperature using a NanoIndenter-XP (MTS Systems Corp.) and NanoSuite 6.0 software. A diamond Berkovich tip was used with the Continuous Stiffness Measurement (CSM) method allowing a continuous measurement of hardness [41]. The tip geometry was calibrated by indenting a fused silica reference sample with known mechanical properties. For each material, load–displacement data from 5 × 5 arrays indents (with 50 μm spacing between the indents) were acquired with a strain rate of 0.05/s and analysed based on the method in [41]. Majority of indents were within grains, avoiding the effect of grain boundaries. At least 3 grains were indented respectively in unirradiated and irradiated zone in each sample to avoid orientation effects.

2.5. Microstructure characterisation

Transmission electron microscopy (TEM) and atom probe tomography (APT) specimens were prepared from the irradiated FNAT-Fine and FNAT-Coarse samples using a Focused Ion Beam (FIB) equipped on an FEI Quanta 3D field emission gun (FEG) dual-beam SEM. The lift-out and thinning were conducted using 30 kV Ga^+ ions and the sample was finally cleaned using 5 kV and 2 kV ions. The characterisation of microstructure and irradiation defects was performed using a 200 kV FEI Tecnai F20 equipped with FEG. Diffraction mode and Dark-Field (DF) mode were employed to analyse the phase structure and distribution. Scanning TEM high-angle annual dark field (STEM-HAADF) mode with a relatively low collection angle was used to obtain both defect and mass contrast. STEM-EDS was conducted at tilt α≈15° using an Oxford INCA EDS instrument. High-resolution Scanning Transmission Electron Microscopy (HR-STEM) and atomic-scale EDS mappings were performed using a probe-corrected Thermal Fisher Themis TEM operating at 300 kV at the Nanoscale Materials Characterization Facility (NMCF) at University of Virginia. A tiling method was used to denoise and construct the HR-STEM/EDS map [42]. the 4D-STEM experiments were performed using the double-aberration-corrected TEAM I TEM operating at 300 kV at the National Centre for Electron Microscopy (NCEM) at Lawrence Berkeley National Laboratory (LBNL). APT measurements were conducted in a Cameca LEAP 5000 XR instrument, either in voltage mode (pulse rate of 250 kHz, pulse fraction of 0.2) in laser mode (laser energy of 50 pJ, pulse fraction of 0.2) with a sample temperature of 50 K and a target evaporation rate of 0.5%. Data reconstruction and analysis were carried out using Cameca AP Suite 6.3 software. The reconstruction was conducted based on the voltage evolution with an image compression factor of 1.65 and a k factor of 3.3. The composition of the matrix and primary precipitates (intermetallic) was measured from an atom-count weighted average of three regions of interest (ROIs). The uncertainty is the standard deviation. The composition of secondary precipitates in FNAT-Coarse was obtained from the only secondary precipitates. The volume fraction of the intermetallic precipitates was determined by Lever rule by performing the linear regression to ($C_{n,i}$-$C_{mat,i}$) and ($C_{ppt,i}$-$C_{mat,i}$), where $C_{n,i}$ is the nominal composition of the element i, $C_{mat,i}$ is the matrix composition and $C_{ppt,i}$ is the intermetallic precipitate composition (Table 1). In FNAT-Coarse, the secondary precipitates has similar composition as the matrix (Table 1), which was considered as part of the matrix for the volume fraction calculation. The nearest neighbor distance (NND) distribution and radial distribution function (RDF) analysis were performed in representative ROI in the matrix and primary precipitates using the NND function and RDF function implanted in AP Suite. NND analysis used the parameters of d_{max} from 2–4 nm and d_{step} = 0.02 nm with various order (O = 1/10/50/100). RDF between Ni and other elements in the matrix and precipitates were calculated with a pin size of 0.1 nm over 5 nm. Results were displayed with normalised concentration.

2.6. Computational details

First-principles calculations were performed using the Vienna ab initio simulation package (VASP) [43,44], implementing the projected augmented wave (PAW) method [45,46]. Exchange-correlation interactions were described using the Perdew-Burke-Ernzerhof (PBE) formulation of the generalised gradient approximation (GGA) [47]. A plane-wave basis set with a cutoff energy of 400 eV was employed. The

Table 1
Phase composition measured by APT in FNAT-F and FNAT-C.

		Concentration (at%)			
		Fe	**Ni**	**Al**	**Ti**
FNAT-F	Matrix	86.8 ± 0.7	4.8 ± 0.1	3.7 ± 0.3	4.6 ± 0.2
	$L2_1$ Precipitate	21.8 ± 0.1	35.5 ± 0.1	21.2 ± 0.1	21.3 ± 0.1
FNAT-C	Matrix	91.7 ± 0.5	2.6 ± 0.2	2.2 ± 0.2	3.4 ± 0.2
	$L2_1$ Precipitate	15.6 ± 0.1	37.3 ± 0.4	23.7 ± 0.3	23.4 ± 0.3
	2nd precipitate	90.7	2.1	2.9	4.2

Methfessel-Paxton scheme (first order) with a smearing width of 0.1 eV was utilised for treating partial orbital occupancies. All calculations incorporated spin polarisation. For the pristine bulk structure, full geometrical optimisation was performed, allowing relaxation of atomic positions, supercell volume, and shape. In contrast, for supercells with planar faults, atomic positions were optimised only along the z-axis while maintaining fixed cell volume and lattice parameters [48]. Convergence criteria were set to 1×10^{-5} eV/atom for electronic self-consistency and 0.02 eV/Å for ionic forces. The Brillouin zone was sampled using a $4 \times 4 \times 2$ k-point mesh. The anti-phase boundary (APB) energy calculations were performed using supercells of B2 Ni(Al,Ti) and $L2_1$ Ni_2AlTi, each containing 144 atoms, as illustrated in Fig. S2 (Atomic configurations of B2 and $L2_1$ structures for APBE calculations). The pristine configurations of B2 Ni(Al,Ti) and $L2_1$ Ni_2AlTi are shown in Fig. S2(a,c), respectively. Through displacement along $\frac{1}{2}[1\bar{1}1]$ direction, $\frac{1}{2}<111>\{110\}$ APBs are created in both structures, as depicted in Fig. S2(b,d).

3. Results and discussion

3.1. Design and microstructure of FNAT alloys

FNAT-Fine and FNAT-Coarse alloys both consist of a disordered-bcc phase (A2) and an ordered-bcc phase ($L2_1$) with a lattice misfit of about 2.0% by synchrotron X-ray diffraction (SXRD) pattern in Fig. 1b (details see Fig. S3 and Table S2). Transmission electron microscopy shows that FNAT-Fine comprises an A2 matrix and cuboidal $L2_1$ precipitates with an average size D of 62±26 nm (Figure 1(c-e)). In FNAT-Coarse, the $L2_1$ precipitates show a slightly rounded cube shape with an average size of 280±169 nm (Figure 1(g, h)). The composition of the matrix and precipitates measured by atom probe tomography (APT) are given in Table 1. Element distribution in Fig. 1f and Fig. 1j indicates that the matrix is Fe-rich, and the precipitates have a close stoichiometry to an intermetallic $(Ni, Fe)_2AlTi$, in line with their A2 and $L2_1$ structure. Both alloys share similar element partitioning, with a slight increase of Fe in the matrix in FNAT-Coarse due to ageing. and secondary precipitates are observed inside. In the $L2_1$ precipitate of FNAT-Coarse, secondary Fe-rich precipitates are observed, exhibiting an A2 structure with a similar composition to the matrix (Figure 1(i, j). The secondary precipitates have disc morphology lying on {100} planes. This hierarchy, A2-$L2_1$-A2, is different from other Fe-Ni_2AlTi alloys with Ti content up to 5 at.%, which were reported to be only A2-$L2_1$ or A2-$L2_1$-B2-ABP (anti-phase boundary) or A2-$L2_1$-B2 [21,34,49]. The area fraction of the intermetallic precipitate measured using scanning electron microscopy (SEM) is about 50% in both alloys, in line with the volume fractions measured by APT using the Lever rule, respectively 52% and 51% in FNAT-Fine and FNAT-Coarse. (Fig. S4). In both alloys, the precipitate-matrix interfaces are the dominant sink for point defects over grain boundaries due to the coarse grain size > 400 μm (Table 2). Based on the formula by Brailsford and Mansur [50], the sink density provided by the matrix-precipitate interface was approximated as follows:

$$S_p = 2\pi ND$$

with D the average size of precipitates and N the number density deduced from the volume fraction and to be 8.5×10^{14} m^{-2} in FNAT-Fine and 4.2×10^{13} m^{-2} in FNAT-Coarse. Due to the low defect mobility in intermetallic, the additional interface area of the secondary Fe-rich precipitates inside the primary precipitates was not taken into account here.

3.2. Suppression of radiation-induced hardening

To evaluate the irradiation behaviour, the Fe ion irradiation experiment was performed at 300 °C followed by nano-indentation, as illustrated in Figure 2(a,b), so that the irradiated zone and unirradiated zone experienced the same heat treatment at 300 °C during the irradiation. Fig. 2c is an area on the irradiated FNAT-Fine alloy where nano-indentation arrays can be identified in both regions. The nano-indentation hardness was shown as a function of the indentation depth for the unirradiated and irradiated zones in FNAT-Fine, FNAT-Coarse and Eurofer97, plotted respectively in Figure 2(d-f). To avoid artefacts, such as from the indenter tip geometry, surface contamination and polish hardening, data from depths less than 80 nm are not considered. In all curves, the hardness H decreases with the contact depth h, which has been well known as an indenter size effect [51]. Both curves converge to the same value for nano-indents deeper than 1000 nm beyond the radiation damage profile, read as the bulk alloy's hardness. Within the damage profile, however, an apparent increase in hardness is revealed in FNAT-Coarse and Eurofer after irradiation. At the same time, the curves in FNAT-Fine remain similar, with no change after irradiation.

To further determine the hardness of the irradiation damage layer, H^2 was plotted over $1/h$ in Figure 2(g,j) based on the model by Nix-Gao [52] and the method by Kasada et al. [53]. H^2 versus $1/h$ should follow the equation:

$$H^2 = {H_0}^2\left(1+\frac{h^*}{h}\right)$$

Where H_0 is the hardness at infinite depth, h^* is a characteristic length as a function of the material and the indenter shape. In all three alloys, the data from the unirradiated zones present an excellent linearity, reflecting a constant hardness of the bulk alloy. The hardness of the unirradiated alloys, H_{unir}, as the square root of the intercept of the curve and are indicated in Table 3. The hardness values fitted using Nix-Gao model are consistent with the direct hardness measurement at h > 1000 nm. As for the irradiated zone, the hardness of irradiated areas at h > 1000 nm, i.e. probing beyond the damage range, are in excellent agreement with the unirradiated values, ensuring the hardness measurement's reliability. Finally, the hardness between 80–200 nm showed good linearity and was used to determine the hardness of irradiated layer, denoted as H_{ir}, to reduce the contribution of unirradiated substrate on the measurement. The H_{ir} values are given in Table 3. Thus, the irradiation hardening increments Δ_H are −0.05 GPa, 1.0 GPa and 0.7 GPa for FNAT-Fine, FNAT-Coarse and Eurofer, respectively. FNAT-Fine exhibited no significant change in hardness-depth profiles (*Figure 2*(d)), though the fitted characteristic hardness decreased marginally. The RIH in FNAT-Fine alloy is strongly reduced compared to its coarse precipitate counterpart and the reference steel.

The irradiation hardening increment for the three alloys was calculated and depicted as a function of sink strength in Fig. 3. Additionally, we have included data from various ferritic and ODS steels that show the increase in irradiation hardening ΔH or yield strength $\Delta\sigma_y$ versus sink strength [5–9,54–56]. Yield strength is converted into hardness using

Table 2
Measured size, volume fraction and calculated number density of precipitates in FNAT alloys with total sink strength S_{total} as the sum of precipitate-matrix interface S_p and grain boundaries, S_g.

Alloys	Precipitate size (nm)	Volume fraction	Number density N (m^{-3})	S_p ($\times 10^{13}$ m^{-2})	S_g	S_{total} (m^{-2})
FNAT-Fine	62	0.52	2.2×10^{15}	85	0.012	8.5×10^{14}
FNAT-Coarse	280	0.52	2.4×10^{13}	4.2	0.012	4.2×10^{13}

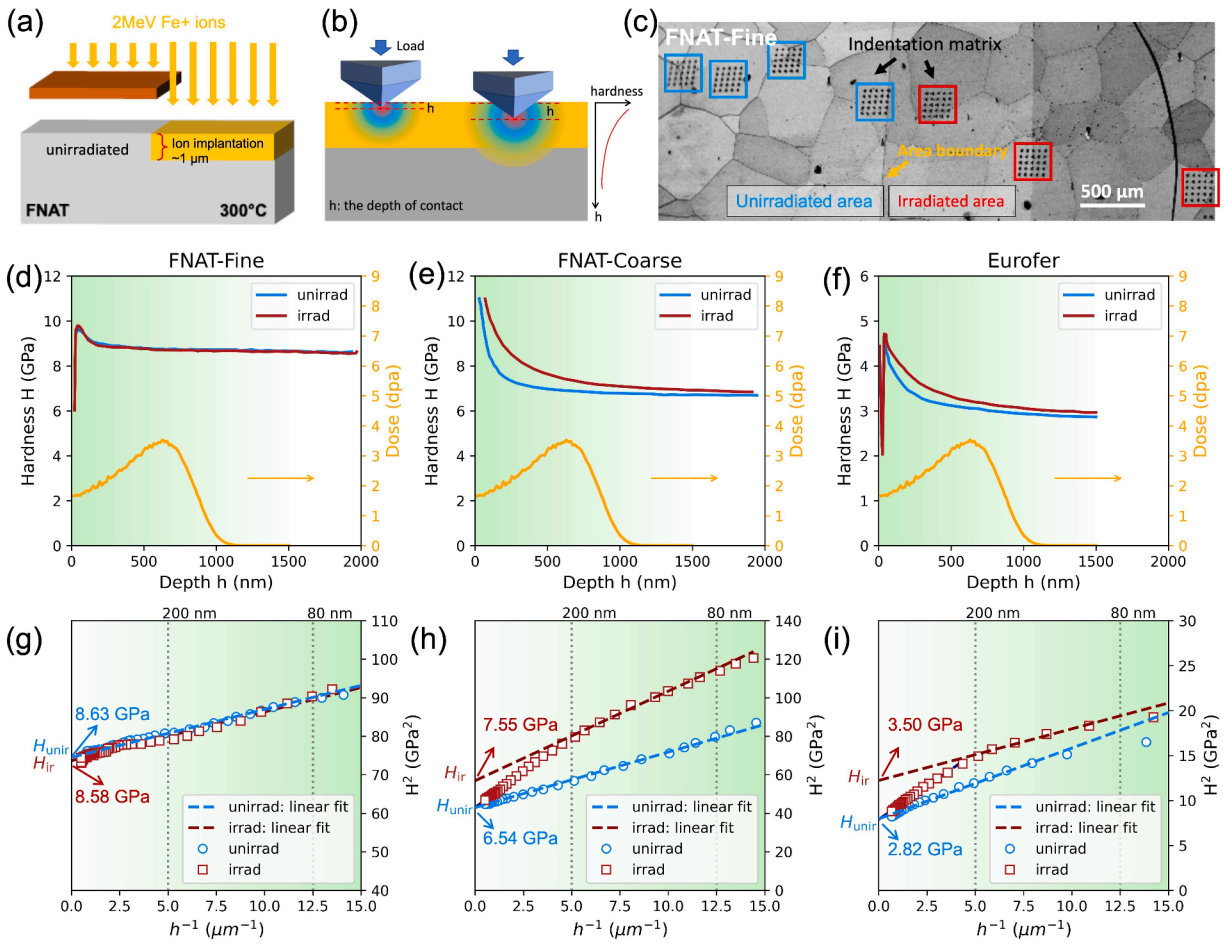

Fig. 2. Irradiation experiment and hardness measurement by nano-indentation. Schema showing (a) the irradiation and (b) nano-indentation experiments with (c) backscattering scanning electron microscope image of the indentation traces on FNAT-Fine samples. The depth, h and hardness, H, relationship by continuous stiffness measurement technique from the unirradiated area (blue) and irradiated area (red) in (d) FNAT-Fine, (e) FNAT-Coarse and (f) Eurofer with the radiation damage profile (orange) showing the radiation-induced hardening. The relationship between h^{-1} and H^2 based on Nix-Gao model in (g) FNAT-Fine, (h) FNAT-Coarse and (i) Eurofer for the determination of the characteristic hardness using data in the range of 80–200 nm.

Table 3
Characteristic hardness of each alloy before and after irradiation from Nix-Gao model fitting.

Alloys	H_{unir} (GPa)	H_{ir} (GPa)	$\Delta H = H_{ir} H_{unir}$ (GPa)
FNAT-Fine	8.63	8.58	~−0.05
FNAT-Coarse	6.55	7.54	~+1.0
Eurofer	2.82	3.50	~+0.7

the empirical conversion formula $\Delta H = \Delta\sigma_y/289.17$ for ferritic steels with ΔH in GPa and $\Delta\sigma_y$ in MPa [57]. Although the irradiation type and mechanical testing methods are varied in literature, Fig. 3 provides a qualitative comparison across different materials with various sink strengths. A consistent trend emerges among the two FNAT alloys, revealing that the RIH is significantly lower when compared to other ferritic alloys. It is worth highlighting that the sink strength in FNAT-Fine reaches approximately 10^{15} m^{-2}, placing it close to ODS steels. This notable resistance to RIH can be attributed to the high interface area of FNAT-Fine. However, it is essential to acknowledge that the sink strength of FNAT-Fine is lower than that of ODS steels, suggesting the involvement of other mechanisms in its performance, which requires further characterisation of the irradiated microstructure.

3.3. Distribution of dislocation loops and hardening mechanism

Radiation-induced structural defects such as dislocation loops and precipitates have been known as sources of RIH. However, dislocation loops are observed. The on-zone [001] STEM Low Angle Annular Dark Field (LAADF) image in Fig. 4a reveals the presence and distribution of radiation-induced dislocation loops in FNAT-Fine. As no loop is observed in regions beyond the damage layer, the effect of FIB damage on the microstructure is excluded. As depicted in Fig. 4b, the observed dislocation loops are predominantly present within the damage range, specifically in the central regions of precipitates, while being noticeably absent in the matrix. Quantitatively, the number density of dislocation loops is measured as 2.2×10^{21} m^{-3}, with an average size of 16 nm. Their Burgers vectors were identified as a_0<110> or a_0<100> with a_0 being the lattice parameter using invisibility criteria (Fig. S5 and Table S3) [58]. In intermetallics with $L2_1$ structure, dislocations with Burgers vectors of both a_0<110> and a_0<100> were observed after creep testing [40]. Dislocation loop nature determination in Fig. S6 suggested these loops were interstitial-type. The observed dominance of interstitial loops aligns with the low vacancy mobility in intermetallics at such a low temperature (300 °C). In FNAT-Coarse, dislocation loops are smaller (~7 nm in diameter) (see Fig. S7). Due to the microstructure complexity, the number density is estimated to be $>9 \times 10^{21}$ m^{-3} counting only recognisable loops. Many loops are trapped at interfaces without being annihilated.

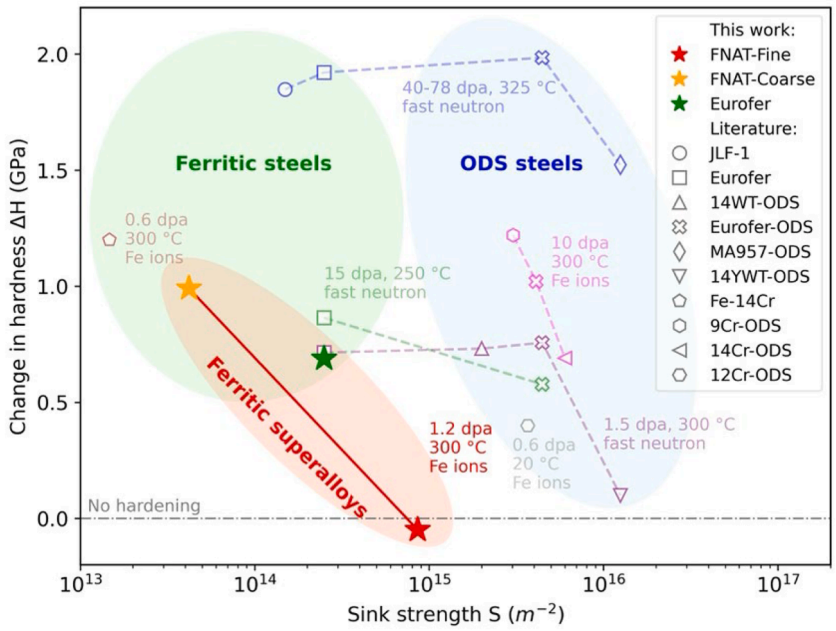

Fig. 3. Radiation-induced hardening of model IDS alloy FNAT and other materials. Effect of initial sink strength on the radiation hardening of FNAT and some steels including conventional low-activation ferritic/martensitic steels (the Japanese low-activation ferritic JLF-1 and EUROFER) and several ODS steels. Data of sink strength from [5–9,54] and data of change in yield strength from [55,56].

In general, dislocation loops act as obstacles for dislocation movement, thus increasing yield strength and hardness. The dispersed barrier hardening model is developed to estimate the hardness increment owing to dislocation loops [3]:

$$\Delta H = \alpha M \mu b n \sqrt{Nd}$$

with α is the obstacle strength [7], $M = 2.9$ the Taylor factor for bcc materials, $\mu = 80$ GPa the shear stress of bcc iron, $b = 0.249$ nm, the Burgers vector of $a_0/2 < 111 >$ dislocations with a_0 the lattice constant, $n = 3$ a conversion factor between hardness H (in GPa) and yield strength σ (in GPa) as $H = n\sigma$. N and d are the average number density of loops and size respectively. Depending on the value of α varying from 0.2 to 1.44 [3,7], here, an increase of hardness is calculated to be 0.2–1.2 GPa, contrasting with the observations where no RIH is detected. It should be noted that Orowan bypassing is the common mechanism for precipitates larger than tens of micro-meters, as shown in B2 or $L2_1$ precipitates strengthened ferritic alloys [59–61], and shearing of ordered-bcc phases typically occurs at smaller sizes, e.g., < 10 nm in bcc-superalloys [62], due to the high anti-phase boundary energy in ordered-bcc phases [63],. Strengthening contribution analysis in the current alloy system also implies Orowan bypassing as the operative mechanism in both FNAT alloys, owing to the large size of precipitates ~ 60 nm, see Fig. S8, though, in FNAT-Fine, precipitate shearing could happen in some small precipitates. Essentially, this mechanism dictates that, during deformation, dislocations tend to bow around precipitates rather than cutting through them. Consequently, the formation of dislocation loops within precipitates is expected to have minimal influence on the overall dislocation mobility and the difference in RIH resistance cannot be attributed to a transition between shearing and Orowan mechanisms, as both alloys share the same underlying deformation mode.

The coherent interface decorated by interfacial dislocations act as recombination sites for these dislocation loops as shown in the schematic in Fig. 4c. The effective role of the interfaces in suppressing defect formation in the matrix and proximity of precipitates is believed to be attributable to the misfit and high strain field around the interface. Using 4D-STEM techniques, the strain distribution in FNAT-Fine is captured in Figure 4(e,f). Note that the lattice in the precipitate was taken as the reference lattice for strain mapping. As the matrix and precipitates have a cube-cube orientation relationship with a lattice misfit of ~1.5%, the lattice at an interface is mainly a longitudinal dilatation or compression. Notably, the matrix side is subjected to a compression field, while the precipitate side is subjected to a tension field, related to the larger lattice parameter of the $L2_1$ structure compared to the A2 structure. Although the effects of strain field on the dislocation loop formation are not well benchmarked, it has been revealed that strain field can change the microstructure development under irradiation, affecting materials' creep behaviour and void swelling [64–66]. It was found that the radiation-induced loops can be suppressed under compression while tension boosts the loop formation or accelerates microstructure evolution [64,67]. The compression field, thus, should play a favourable role in suppressing the loop formation. Furthermore, 4D-STEM has been found effective in detecting local strain variation around a 2D structure, such as the stacking fault inside radiation-induced dislocation loops [63]. As shown in Figure 4(g,h), a strain concentration peak is revealed at the interface on the precipitate side with a long tail from the local maximum to 5–10 nm into the precipitates. This peak is counterintuitive for a continuous matter, as a monotonic lattice parameter transition will not lead to such a peak. One possible origin is the misfit dislocations at the interface causing local stresses. Such a long-range strain field may enhance the point defect mobility at the proximity of the interface, which leads to defect depletion, as observed in Fig. 4b

Apart from the role of the interface in enhancing defect recombination, the defect depletion close to the interfaces may be evidence that the presence of fine precipitates with a high density of interfaces can suppress the production of overall primary radiation damage. This agrees with a newly modified Norgett, Robinson and Torrens (NRT) formalism accounting for the microstructure, which revealed that factors like precipitate size and compositions strongly affect the damage experienced by each phase in a bcc ferritic superalloy [68]. In all, by comparing the FNAT-Fine and FNAT-Coarse, which have similar interface properties but different densities, their RIH behaviour underscores the IDS design where the coherent semi-coherent precipitate-matrix interfaces offer an efficient way to enhance the radiation resistance of a bcc matrix.

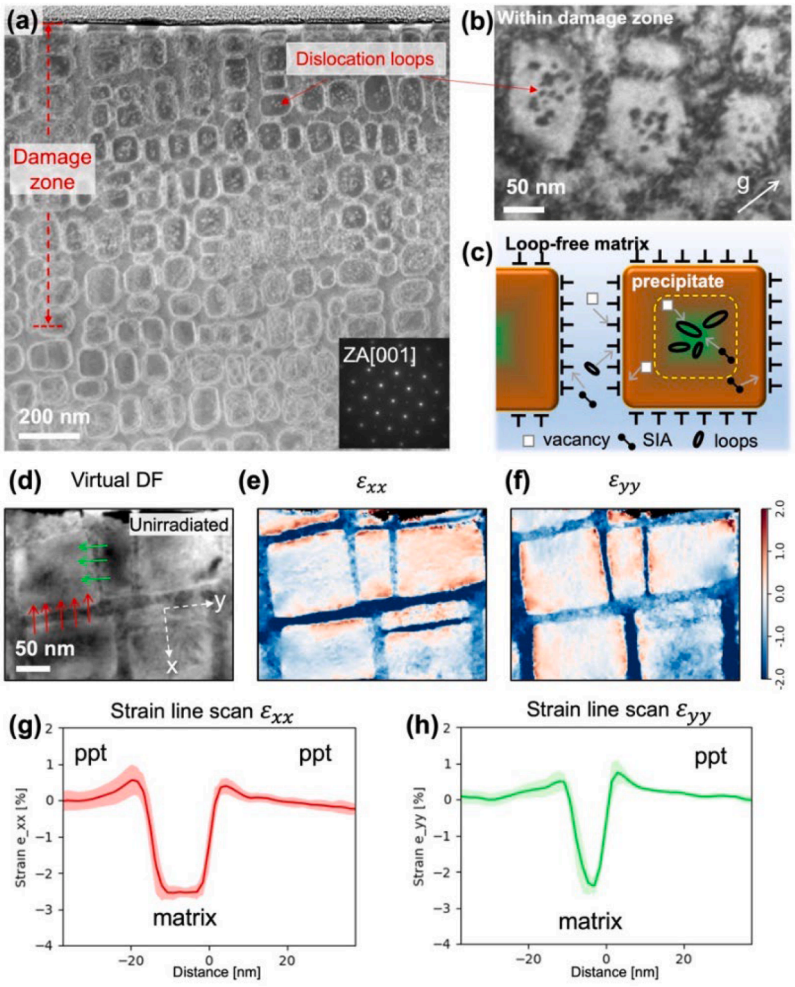

Fig. 4. TEM observation of irradiated microstructure in FNAT-Fine. (a) STEM-LAADF image along zone axis [001] showing an overview microstructure from irradiated layer to unirradiated area. (b) Kinematic bright-field images under a two-beam condition with diffraction $g \leq 200>$ ($s_g>0$) close to zone axis ⟨001⟩ within the damage layer. In irradiated precipitates, radiation-induced dislocation loops within the precipitates are observed. (c) Schematic diagram of point defects diffusion in the matrix and precipitates. (d) 4D-STEM virtual dark-field image along the zone axis [001] in unirradiated FNAT-Fine samples with corresponding (e) ε_{xx} and (f) ε_{yy} strain maps (ε_{xx} and ε_{yy} are longitudinal strain along the x and y axis respectively). (g) and (h) show the line scan of strain as indicated in (d).

3.4. *Partial disordering of $L2_1$*

The softening in FNAT-Fine after irradiation is counterintuitive to the observation of dislocation loops. After irradiation, the phase composition remains almost constant (Fig. S9), with a slight trade of Ni, Al and Ti in the matrix with the Fe in the intermetallic precipitates. APT results suggest a slight increase in the intermetallic volume fraction in irradiated samples likely due to the variation of volume fraction inside the sample as no significant change in precipitate size is evidenced by the TEM observations (Fig. 4a and Fig. S7). Additionally, APT analysis fails to show radiation-induced clustering/precipitation in both matrix and precipitates (an example APT dataset in Fig. 5a), where no clustering contrast is visible and the experimental nearest neighbour distance (NND) distributions agree with the random ones even with a high order $O = 100$ (Fig. 5b). Further radius distribution function (RDF) of all elements to Al shows normalised concentrations close to 1 at distance $>$ 2 nm (Fig. S10), which also suggests an absence of clusters in FNAT-Fine after irradiation.

Instead, a long-range phase transformation of the $L2_1$ precipitates occurred. The irradiation stability of the long-range ordering of intermetallic and ceramics has received long-standing attention [69,70]. In intermetallic-strengthened alloys such as ferritic steels and zirconium alloys, (ion) irradiation has been shown to induce complete disordering and eventual amorphisation of intermetallic phases [71–74], influencing the radiation and corrosion resistance. In precipitate-hardened Ni superalloys such as Inconel 718, both ion and neutron irradiation-induced disordering and dissolution of precipitates which caused softening and was believed to counterbalance the hardening induced by radiation-induced defects [29,75]. In FNAT-Fine, the TEM dark field image in Fig. 5c is generated from a $L2_1$ superlattice reflection along the zone axis (ZA) [011] and is overlapped with the profiles of radiation damage and implantation, where a disappearance of the $L2_1$ structure is revealed within the radiation damage zone ($<$ 900 nm). 4D-STEM phase maps in Fig. 5d indicate the existence of B2 structure within the damage zone, as confirmed by the STEM diffraction patterns along $<112>$ zone axis. Within the $L2_1$ depletion regions, B2 superlattices reflections are observed while, in deeper areas, $L2_1$ superlattices reflections appear. The depth of $L2_1$ denuded regions aligns well with the damage profile before the peak of self-ion implantation. Another TEM sample from unirradiated regions (masked during irradiation) shows $L2_1$ with the same diffraction pattern as the deep area of an irradiated sample, ensuring that this change of diffraction patterns is not due to any artefacts, such as surface treatment or heat treatment during irradiation. The same phenomenon is also observed in FNAT-Coarse (Fig. S11). Therefore, we can conclude that the initial long-range ordered $L2_1$ structure is disordered into a lower-ordered B2 structure under irradiation. To unravel the disordering path, HR-STEM images coupled with EDS were performed (Figure 5(e-h)), indicating that the

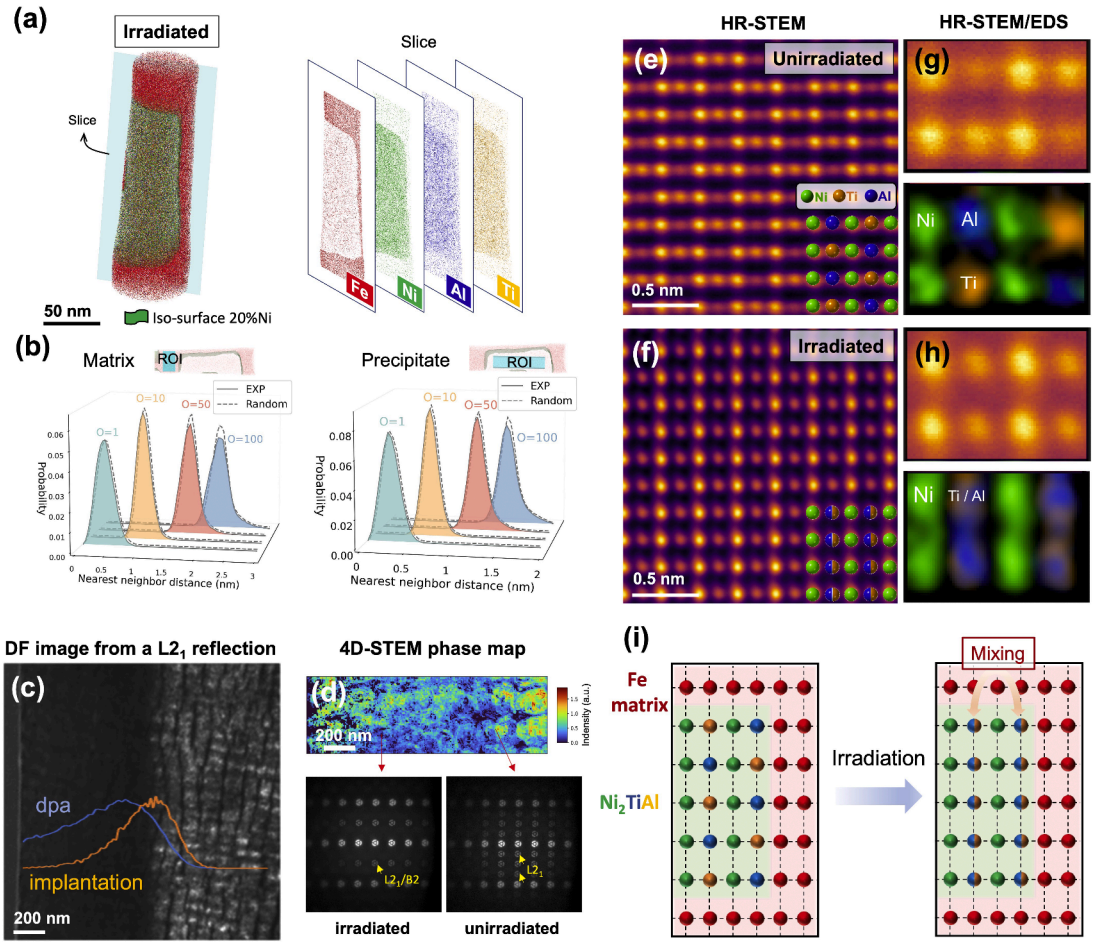

Fig. 5. Disordering of L2$_1$ structure in FNAT-Fine after irradiation at 300 °C. (a) APT element map with a selected slice of 2 nm thickness. (b) Nearest neighbor distribution with various order O for a volume of interest inside the matrix and the precipitate. (c) Dark-field (DF) image using $a < 111 >$ reflection of L2$_1$ structure. Damage and implantation profiles are overlapped with the image. (d) 4D-STEM phase maps showing the sum of the L2$_1$ reflections intensity (upper hot map) and STEM diffraction patterns from the irradiated area and unirradiated area (lower). Patterned apertures were used as described in this study [76]. The specimen is tilted along ⟨112 ⟩ zone axis. High-resolution (HR) STEM/HAADF images in a precipitate from (e) an unirradiated and (f) an irradiated sample with (g) and (h) the corresponding HR STEM/EDS maps. The contrast is coloured using inferno colourmap in python. Fe was omitted in spectrum analysis due to signals from the instruments. (i) scheme depicting the mixing of the Ti and Al sublattice in the L2$_1$ structure under irradiation.

two sub-lattices, Ti and Al, in the initial L2$_1$ structure have been mixed after irradiation. The disordering from L2$_1$ to B2 is thus attributed to the mixing of Al-rich sublattice and Ti-rich sublattice under irradiation, which forms a B2-Ni(Al,Ti) compound. Based on the corresponding strain maps (Fig. S12), this sublattice mixing induces minimal lattice parameter changes or misorientations.

3.5. *Phase stability under irradiation: A2-B2 reversible transformation*

The stability of the L2$_1$ structure and its disordering kinetics under irradiation were further investigated using in-situ ion irradiation from room temperature to 500 °C. 1.17 MeV or 900 keV Kr^{3+} ions were used to increase the dose rate, while the high energies of Kr^{3+} ions ensure that the injected atoms can be neglected. Fig. 6a superlattice reflections disappear, leaving only B2 reflections, as a function of irradiation temperature. The partial disordering can be observed when temperatures are lower than 500 °C and are accelerated by decreasing the temperature. It is worth noting that no complete disordering from B2 to A2, or amorphisation, was observed, and the B2 structure remains stable under irradiation from RT to 450 °C within the dose range up to 1.5 dpa.

Another direct effect from the disordering is the change of antiphase boundary (APB) energies, which play a crucial role in determining dislocation mobility and plasticity, thereby significantly influencing the strength and ductility of intermetallic compounds. In BCC intermetallics, APB formation typically occurs through shearing within {110} planes [77,78]. The APB energies were calculated using the equation [79]: $\gamma_{APB} = \frac{E_{APB} - E_0}{2A}$, where E_{APB} and E_0 are the energies of the supercell with and without APBs, respectively, and A denotes the cross-sectional area of the APB. To account for statistical variations, we generated three simulation cells for B2 Ni(Al,Ti), each with different random distributions of Al and Ti atoms in their sublattice. The calculated APB energies are presented in Fig. 6b, alongside γ_{APB} values for B2 NiAl and NiTi structures for comparison. Our calculated APB energy for B2 NiTi shows excellent agreement with previous findings [78]. The results further demonstrate that the APB energy of B2 Ni(Al,Ti) falls between those of B2 NiAl and NiTi, following a rule of mixture behavior. Notably, the L2$_1$ structure exhibits substantially higher APB energies compared to the B2 structures. This elevated APB energy in the L2$_1$ phase suggests enhanced resistance to dislocation glide across APBs, resulting in reduced dislocation mobility. This finding correlates well with experimental observations, where transformation to the B2 phase after irradiation induces less hardening effects compared to their pristine L2$_1$ counterparts, aligning with the aligns with behavior in analogous systems, such as oxide dissolution in ODS alloys [80] and γ' (Ni_3Al) disordering in Ni-based superalloys [81].

Phase stability under irradiation has been a longstanding topic and

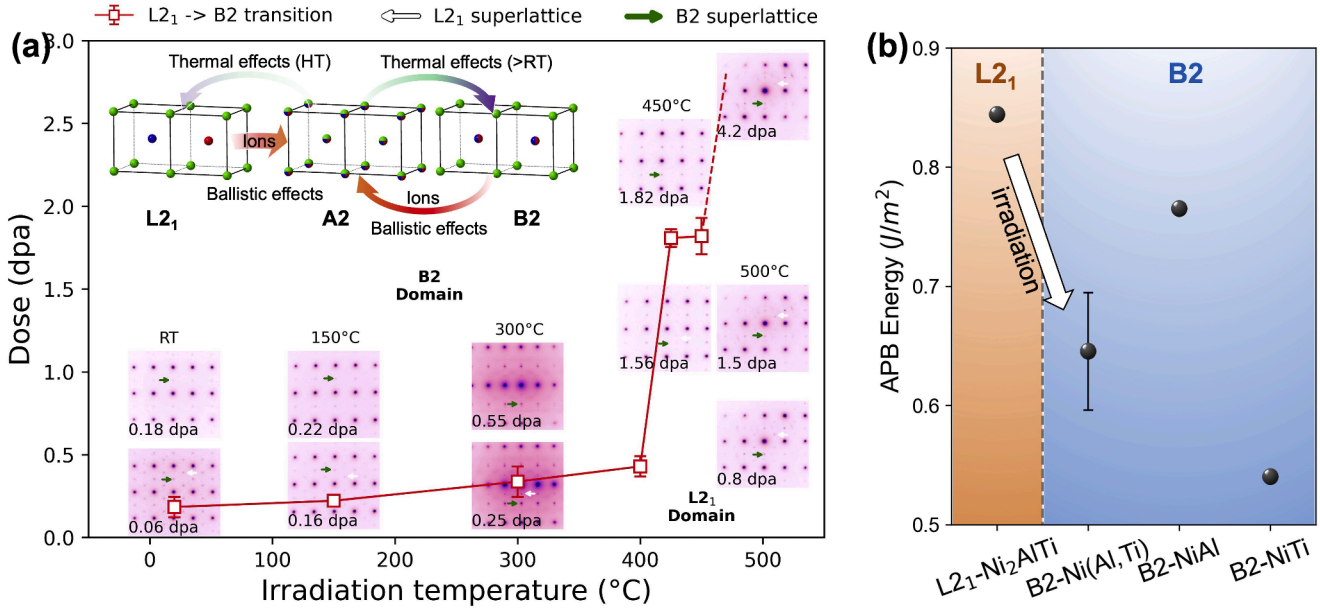

Fig. 6. Competition of ballistic effects and thermal effects on the structure ordering and antiphase boundary energies. (a) Threshold dose for reduction of structure ordering from $L2_1$ to B2 in FNAT determined by in-situ ion experiments. Inset schematic showing the structure disordering by ballistic effects and reordering by thermal effects. Error bars represent the standard error of the measurements. (b) Comparison of APB energies in B2 NiAl, B2 Ni(Al,Ti), B2 NiTi, and $L2_1$ Ni_2AlTi intermetallic compounds. The APB energies for B2 Ni(Al,Ti) were calculated using three independent simulation cells with distinct random distributions of Al and Ti atoms in the sublattice. Error bar is from different configuration.

can be considered a result of two competing effects. The energetic displacement cascades caused by irradiation can lead to atomic mixing, causing precipitates to dissolve or disorder through ballistic processes and creating uniform solid solution structures. Conversely, when atomic diffusion is augmented by irradiation and thermal effects, it tends to promote the nucleation and growth of precipitates, especially in cases where the thermodynamic equilibrium state involves a two-phase or multi-phase condition. A generic way was proposed to describe the contribution of ballistic effects to interdiffusion and to study the mixing and unmixing in the presence of such effects. To determine the stable state of the material, the irradiation can be considered as an increase in the temperature, which depends on the irradiation parameters and material properties [70]. However, from the phase diagram of the quaternary system Fe-Ni-Al-Ti [82] and in Fig. S13, an increase in temperature from an $L2_1$ region will lead to either (i) a fully $L2_1$ structure, (ii) the coexistence of amorphous zones (Liquid) and $L2_1$ ordered compounds or (iii) complete amorphisation, which is controversial to the present observations. Here, we believe that there is simultaneous disordering and reordering under irradiation, as shown in Fig. 6. The strong ballistic effects of heavy ion irradiation are known to induce local atom mixing and disordering by thermal spikes, replacement collision sequences and random vacancy-interstitial recombination [83]. Afterwards, the reordering into a fully recovered $L2_1$ structure when $T > 500$ °C or into an intermediate state of order (i.e. B2) when $T < 500$ °C takes place. The reordering is accelerated with temperature, suggesting that the thermally activated migration of point defects may play a dominant role in the reordering, as evidenced by the resistivity experiments in other materials [84–86]. It is worth noting that reordering to B2 occurs at ambient temperature, as B2 is known to readily form from A2/liquid. This continuous disordering-reordering process offers several advantages in radiation resistance. At a wide range of temperatures, it may offer an additional point defect recombination mechanism in ferritic superlattice steels to suppress the accumulation of vacancies, which is known to lead to void swelling [28]. Also, the ability of intermetallic to retain its crystalline structure could avoid significant volume changes, such as swelling due to radiation-induced amorphisation, which is known in covalent crystals like ceramics. Finally, the partial disordering alters the matrix-precipitate interface from A2/$L2_1$ to A2/B2. Since the cleavage energy of the A2/B2 interface is lower than that of the A2/$L2_1$ interface [87], this partial disordering could result in a less brittle interface.

3.6. *Recovery of radiation-induced $L2_1$-to-B2 transformation by thermal annealing*

Thermal annealing is an effective way to recover radiation-induced damage. To probe the reversibility of the $L2_1$-to-B2 transformation, we conducted in-situ irradiation and annealing experiments up to 1200 °C. In-situ annealing at 500 °C on an irradiated sample for ~2 min fully restored the ordered $L2_1$ structure in the irradiated sample, with the phase remaining stable upon cooling to RT, confirming the reversibility of irradiation-induced disordering (Fig. 7). With reheating, diffraction analysis revealed retained $L2_1$ superlattice reflections up to 1100 °C, demonstrating exceptional thermal stability of the phase. At 1200 °C, both $L2_1$ and B2 superlattice reflections vanished, indicative of precipitate dissolution into a solutionised matrix. Observed additional diffraction spots during heating at 1200 °C were attributed to surface oxidation rather than phase transformation. Residual coarsened precipitates, likely adopting the disordered A2 structure, exhibited no contrast differentiation in HAADF images, consistent with DSC data showing phase transformation completion at 1100–1140 °C (Fig. S14). These findings highlight that annealing above 500 °C enables recovery of the $L2_1$ phase, though precipitate coarsening at elevated temperatures may diminish strengthening effects. While thermal recovery of disordering is achievable, the effectiveness of defect recovery (e.g., dislocation loops) at these temperatures remains uncertain, necessitating further study to evaluate implications for post-annealing mechanical properties.

4. Conclusions

In summary, the early-stage irradiation behaviour of a model intermetallic dispersion-strengthened (IDS) ferritic alloys (FNAT) was investigated. FNAT comprises nanoscale $L2_1$ precipitates within a

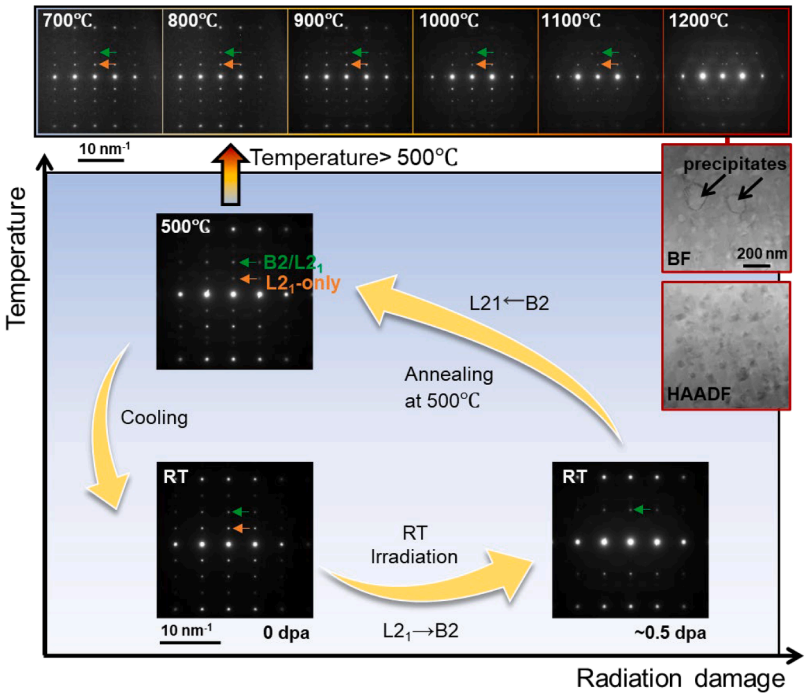

Fig. 7. In-situ annealing experiment to recover $L2_1$-to-B2 disordering in FNAT-Fine.

ferritic A2 matrix, resulting in a high density of semi-coherent interfaces. The nanostructure can be tuned by heat treatment to achieve different precipitate size and density, morphology and hierarchical structure with various interface irradiation sink strengths. An FNAT alloy with an average precipitate size of 62 nm and a sink density in the range of ODS steels has been found to exhibit exceptional resistance to radiation-induced hardening. Advanced microscopy reveals that interfacial strain fields—driven by positive lattice misfit—critically suppress dislocation loop formation by promoting defect recombination at matrix-precipitate interfaces. Additionally, irradiation-induced partial disordering of $L2_1$ precipitates into B2 structures reduces antiphase boundary APB energy, introducing a competing softening mechanism that offsets hardening from dislocation loops. This softening mechanism—evidenced as the sole significant microstructural change in the absence of voids, defect clusters, or elemental segregation—aligns with behaviour in analogous systems such as ODS and Ni-based superalloys. This dual dynamic—interface-mediated defect suppression combined with precipitate disordering—underpins the alloy's exceptional resistance to irradiation hardening at low doses. By linking microstructure (lattice misfit, phase stability) to radiation tolerance, this work advances the design of IDS alloys as potential alternatives to ODS steels for nuclear applications, offering superior manufacturability without compromising defect sink efficacy.

Future efforts should explore long-term microstructural stability under reactor-relevant conditions (e.g., elevated temperatures, higher doses) and quantify the relative contributions of interfacial sinks versus APB energy reduction to irradiation resistance. While this study establishes the early-stage irradiation resistance of FNAT alloys—highlighting interfacial strain fields and $L2_1$ precipitates as critical defect sinks—further investigation is needed to unravel the long-term stability of these strain states and their quantitative efficiency relative to grain or twin boundaries. Future in-situ irradiation experiments coupled with multiscale modelling could elucidate whether interface-dominated defect recombination persists at higher doses or if strain relaxation compromises this mechanism. Notably, the absence of voids here aligns with low-temperature, low-dose conditions, but extending this work to reactor-relevant regimes (e.g., elevated temperatures, higher doses, as in [28]) will test the scalability of FNAT's radiation tolerance. Such efforts would bridge our understanding of emergent microstructural sinks (coherent interfaces, nanoscale intermetallics) with classical defect-engineering principles, accelerating the design of next-generation nuclear alloys.

Data and materials availability

All data are available in the main text or the supplementary materials.

CRediT authorship contribution statement

Kan Ma: Writing – review & editing, Writing – original draft, Visualization, Validation, Software, Methodology, Investigation, Formal analysis, Data curation, Conceptualization. **Pedro A. Ferreirós:** Writing – review & editing, Visualization, Investigation, Formal analysis, Data curation. **Thomas W. Pfeifer:** Writing – review & editing, Visualization, Software, Methodology, Investigation, Data curation. **Robert G. Abernethy:** Investigation, Data curation. **Sophia von Tiedemann:** Writing – review & editing, Investigation, Formal analysis. **Nianhua Peng:** Resources. **Graeme Greaves:** Writing – review & editing, Methodology, Data curation. **Colin Ophus:** Writing – review & editing, Visualization, Validation, Software, Methodology. **Kai Sun:** Writing – review & editing, Investigation. **Anamul H Mir:** Resources. **Lumin Wang:** Writing – review & editing, Supervision, Resources. **Shasha Huang:** Writing – review & editing, Visualization, Software, Methodology, Investigation, Formal analysis, Data curation. **Shijun Zhao:** Writing – review & editing, Validation, Supervision, Resources, Methodology. **Patrick E. Hopkins:** Writing – review & editing, Supervision, Resources, Funding acquisition. **Christopher D. Hardie:** Writing – review & editing, Validation, Supervision, Resources, Project administration, Methodology, Funding acquisition, Conceptualization. **Alexander J. Knowles:** Writing – review & editing, Validation, Supervision, Resources, Project administration, Methodology, Funding acquisition, Conceptualization.

Declaration of competing interest

The authors declare that they have no known competing financial

interests or personal relationships that could have appeared to influence the work reported in this paper.

Acknowledgments

A.J. Knowles gratefully acknowledges funding from EPSRC EP/T016566/1, UKRI Future Leaders Fellowship MR/T019174/1 & MR/Y034155/1, and Royal Academy of Engineering Research Fellowship RF \201819\18\158. A. J. Knowles, C. Hardie and S. von Tiedemann gratefully acknowledge the funding from the NEUtron iRradiatiOn of advaNced stEels (NEURONE) programme via Fusion Futures. A. J. Knowles and K. Ma thank the European Union's Horizon 2020 research and innovation programme under grant agreement No 958418 "COMPASsCO2" (https://www.compassco2.eu). The work at the University of Virginia was supported from the Office of Naval Research, Grant Number N00014-21-1-2477. The atom probe facility at the University of Oxford is funded by EPSRC grant EP/T011505/1, and access was supported by UKRI-NNUF EP/T011351/1 (Call 7 Application 88). K. Ma and A. J. Knowles thank Dr Christina Hofer and Dr Paul Bagot for their support in APT data collection, data analysis and fruitful discussion. The authors also acknowledge the Diamond Light Source UK for time on beamline I11 under proposal CY32708, supported by Dr Sarah Day. Work at the Molecular Foundry was supported by the Office of Science, Office of Basic Energy Sciences, of the U.S. Department of Energy under Contract No. DE-AC02-05CH11231. K. Ma acknowledges the support of Dr Karen Bustillo and Dr Stephanie Ribet on the 4D-STEM experiment. K. Ma and P. A. Ferreirós acknowledge EPSRC grants EP/M028283/1 for funding the MIAMI-2 system construction and EP/X015491/1 for the UKNIBC access scheme. The authors gratefully acknowledge the Centre for Electron Microscopy University of Birmingham for their support & assistance in this work.

Supplementary materials

Supplementary material associated with this article can be found, in the online version, at doi:10.1016/j.actamat.2025.121095.

References

[1] K. Nordlund, J. Keinonen, M. Ghaly, R.S. Averback, Coherent displacement of atoms during ion irradiation, Nature 398 (1999) 49–51.
[2] B.D. Wirth, How does radiation damage materials? Science (1979) 318 (2007) 923–924.
[3] G.S. Was, Fundamentals of Radiation Materials Science: Metals and Alloys, Springer, 2016.
[4] S.J. Zinkle, J.T. Busby, Structural materials for fission & fusion energy, Mater. Today 12 (2009) 12–19, https://doi.org/10.1016/S1369-7021(09)70294-9.
[5] S.J. Zinkle, L.L. Snead, Designing radiation resistance in materials for fusion energy, Annu. Rev. Mater. Res. 44 (2014) 241–267.
[6] M. Klimenkov, R. Lindau, E. Materna-Morris, A. Möslang, TEM characterization of precipitates in EUROFER 97, Progr. Nucl. Energy 57 (2012) 8–13, https://doi.org/10.1016/j.pnucene.2011.10.006.
[7] C. Heintze, F. Bergner, A. Ulbricht, M. Hernández-Mayoral, U. Keiderling, R. Lindau, T. Weissgärber, Microstructure of oxide dispersion strengthened Eurofer and iron–chromium alloys investigated by means of small-angle neutron scattering and transmission electron microscopy, J. Nucl. Mater. 416 (2011) 35–39, https://doi.org/10.1016/j.jnucmat.2010.11.102.
[8] M.K. Miller, K.F. Russell, D.T. Hoelzer, Characterization of precipitates in MA/ODS ferritic alloys, J. Nucl. Mater. 351 (2006) 261–268, https://doi.org/10.1016/j.jnucmat.2006.02.004.
[9] P. Gavoille, A. Courcelle, J.L. Seran, X. Averty, B. Bourdiliau, O. Provitina, V. Garat, D. Verwaerde, Mechanical Properties of Cladding and Wrapper Materials for the ASTRID Fast-Reactor Project, IAEA, International Atomic Energy Agency (IAEA), 2013 p. v. http://inis.iaea.org/search/search.aspx?orig_q=RN:45089554.
[10] D. Gelles, Microstructural examination of commercial ferritic alloys at 200 dpa, J. Nucl. Mater. 233 (1996) 293–298.
[11] P. Dubuisson, R. Schill, M. Hugon, I. Grislin, J. Seran, Behavior of an oxide dispersion strengthened ferritic steel irradiated in Phenix, ASTM International, 1999.
[12] M.B. Toloczko, F.A. Garner, S.A. Maloy, Irradiation creep and density changes observed in MA957 pressurized tubes irradiated to doses of 40–110 dpa at 400–750 C in FFTF, J. Nucl. Mater. 428 (2012) 170–175.
[13] Y. de Carlan, X. Averty, J.-C. Brachet, J.-L. Bertin, F. Rozenblum, O. Rabouille, A. Bougault, Post-Irradiation Tensile Behavior and Residual Activity of Several Ferritic/Martensitic and Austenitic Steels Irradiated in Osiris Reactor at 325 C up to 9 dpa, ASTM Spec. Tech. Publ. 1475 (2006) 67.
[14] E. Materna-Morris, R. Lindau, H.-C. Schneider, A. Möslang, Tensile behavior of EUROFER ODS steel after neutron irradiation up to 16.3 dpa between 250 and 450 °C, Fusion Eng. Des. 98 (2015) 2038–2041.
[15] G.R. Odette, On the status and prospects for nanostructured ferritic alloys for nuclear fission and fusion application with emphasis on the underlying science, Scr. Mater. 143 (2018) 142–148.
[16] S. Zinkle, J. Boutard, D. Hoelzer, A. Kimura, R. Lindau, G. Odette, M. Rieth, L. Tan, H. Tanigawa, Development of next generation tempered and ODS reduced activation ferritic/martensitic steels for fusion energy applications, Nucl. Fusion 57 (2017) 092005.
[17] Z.K. Teng, F. Zhang, M.K. Miller, C.T. Liu, S. Huang, Y.T. Chou, R.H. Tien, Y. A. Chang, P.K. Liaw, New NiAl-strengthened ferritic steels with balanced creep resistance and ductility designed by coupling thermodynamic calculations with focused experiments, Intermetallics. (Barking) 29 (2012) 110–115, https://doi.org/10.1016/j.intermet.2012.05.007.
[18] N.Q. Vo, C.H. Liebscher, M.J. Rawlings, M. Asta, D.C. Dunand, Creep properties and microstructure of a precipitation-strengthened ferritic Fe–Al–Ni–Cr alloy, Acta Mater. 71 (2014) 89–99.
[19] S.-I. Baik, S.-Y. Wang, P.K. Liaw, D.C. Dunand, Increasing the creep resistance of Fe-Ni-Al-Cr superalloys via Ti additions by optimizing the B2/L21 ratio in composite nano-precipitates, Acta Mater. 157 (2018) 142–154, https://doi.org/10.1016/j.actamat.2018.07.025.
[20] D. Bowden, Y. Krysiak, L. Palatinus, D. Tsivoulas, S. Plana-Ruiz, E. Sarakinou, U. Kolb, D. Stewart, M. Preuss, A high-strength silicide phase in a stainless steel alloy designed for wear-resistant applications, Nat. Commun. 9 (2018) 1374.
[21] G. Song, S.J. Hong, J.K. Lee, S.H. Song, S.H. Hong, K.B. Kim, P.K. Liaw, Optimization of B2/L21 hierarchical precipitate structure to improve creep resistance of a ferritic Fe-Ni-Al-Cr-Ti superalloy via thermal treatments, Scr. Mater. 161 (2019) 18–22, https://doi.org/10.1016/j.scriptamat.2018.10.004.
[22] M. Palm, Concepts derived from phase diagram studies for the strengthening of Fe–Al-based alloys, Intermetallics. (Barking) 13 (2005) 1286–1295, https://doi.org/10.1016/j.intermet.2004.10.015.
[23] D.G. Morris, M.A. Muñoz-Morris, Room and high temperature deformation behaviour of a forged Fe–15Al–5Nb alloy with a reinforcing dispersion of equiaxed Laves phase particles, Mater. Sci. Eng.: A 552 (2012) 134–144, https://doi.org/10.1016/j.msea.2012.05.022.
[24] P.A. Ferreirós, P.R. Alonso, P.H. Gargano, P.B. Bozzano, H.E. Troiani, A. Baruj, G. H. Rubiolo, Characterization of microstructures and age hardening of Fe1−2xAlxVx alloys, Intermetallics. (Barking) 50 (2014) 65–78, https://doi.org/10.1016/j.intermet.2014.02.014.
[25] Z.K. Teng, M.K. Miller, G. Ghosh, C.T. Liu, S. Huang, K.F. Russell, M.E. Fine, P. K. Liaw, Characterization of nanoscale NiAl-type precipitates in a ferritic steel by electron microscopy and atom probe tomography, Scr. Mater. 63 (2010) 61–64, https://doi.org/10.1016/j.scriptamat.2010.03.013.
[26] Z.K. Teng, G. Ghosh, M.K. Miller, S. Huang, B. Clausen, D.W. Brown, P.K. Liaw, Neutron-diffraction study and modeling of the lattice parameters of a NiAl-precipitate-strengthened Fe-based alloy, Acta Mater. 60 (2012) 5362–5369, https://doi.org/10.1016/j.actamat.2012.05.033.
[27] R. Jones, F. Di Gioacchino, H. Lim, T. Edwards, C. Schwalbe, C. Battaile, W. Clegg, Reduced partitioning of plastic strain for strong and yet ductile precipitate-strengthened alloys, Sci. Rep. 8 (2018) 1–14.
[28] J. Du, S. Jiang, P. Cao, C. Xu, Y. Wu, H. Chen, E. Fu, Z. Lu, Superior radiation tolerance via reversible disordering–ordering transition of coherent superlattices, Nat. Mater. (2022) 1–8.
[29] J. Hunn, E. Lee, T. Byun, L. Mansur, Ion-irradiation-induced hardening in Inconel 718, J. Nucl. Mater. 296 (2001) 203–209.
[30] D.A. McClintock, M.N. Gussev, C. Campbell, K. Mao, T.G. Lach, W. Lu, J. A. Hachtel, K.A. Unocic, Observations of radiation-enhanced ductility in irradiated Inconel 718: tensile properties, deformation behavior, and microstructure, Acta Mater. 231 (2022) 117889, https://doi.org/10.1016/j.actamat.2022.117889.
[31] C.D. Hardie, C.A. Williams, S. Xu, S.G. Roberts, Effects of irradiation temperature and dose rate on the mechanical properties of self-ion implanted Fe and Fe–Cr alloys, J. Nucl. Mater. 439 (2013) 33–40.
[32] Y. Yang, G.D. Samolyuk, T. Chen, J.D. Poplawsky, A.R. Lupini, L. Tan, L. Ken, Coupling computational thermodynamics with density-function-theory based calculations to design L12 precipitates in FeNi based alloys, Mater. Des. 191 (2020) 108592.
[33] Y. Yang, T. Chen, L. Tan, J.D. Poplawsky, K. An, Y. Wang, G.D. Samolyuk, K. Littrell, A.R. Lupini, A. Borisevich, E.P. George, Bifunctional nanoprecipitates strengthen and ductilize a medium-entropy alloy, Nature 595 (2021) 245–249, https://doi.org/10.1038/s41586-021-03607-y.
[34] G. Song, Z. Sun, L. Li, X. Xu, M. Rawlings, C.H. Liebscher, B. Clausen, J. Poplawsky, D.N. Leonard, S. Huang, Ferritic alloys with extreme creep resistance via coherent hierarchical precipitates, Sci. Rep. 5 (2015) 1–14.
[35] M.J. Rawlings, C.H. Liebscher, M. Asta, D.C. Dunand, Effect of titanium additions upon microstructure and properties of precipitation-strengthened Fe-Ni-Al-Cr ferritic alloys, Acta Mater. 128 (2017) 103–112.
[36] C. Liebscher, V. Radmilović, U. Dahmen, N. Vo, D. Dunand, M. Asta, G. Ghosh, A hierarchical microstructure due to chemical ordering in the bcc lattice: early stages of formation in a ferritic Fe–Al–Cr–Ni–Ti alloy, Acta Mater.. 92 (2015) 220–232.
[37] C. Liebscher, V. Radmilovic, U. Dahmen, M. Asta, G. Ghosh, On the formation of hierarchically structured L2 1-Ni 2 TiAl type precipitates in a ferritic alloy, J. Mater. Sci. 48 (2013) 2067–2075.

[38] Z.K. Teng, C.T. Liu, G. Ghosh, P.K. Liaw, M.E. Fine, Effects of Al on the microstructure and ductility of NiAl-strengthened ferritic steels at room temperature, Intermetallics. (Barking) 18 (2010) 1437–1443, https://doi.org/10.1016/j.intermet.2010.03.026.
[39] R. Darolia, NiAl alloys for high-temperature structural applications, JoM 43 (1991) 44–49.
[40] P.R. Strutt, R.S. Polvani, J.C. Ingram, Creep behavior of the heusler type structure alloy Ni2AlTi, Metallurgic. Trans. A 7 (1976) 23–31, https://doi.org/10.1007/BF02644035.
[41] W.C. Oliver, G.M. Pharr, Measurement of hardness and elastic modulus by instrumented indentation: advances in understanding and refinements to methodology, J. Mater. Res. 19 (2004) 3, https://doi.org/10.1557/jmr.2004.19.1.3.
[42] T.W. Pfeifer, K. Ma, N. Peng, A. Knowles, J. Hachtel, E.R. Hoglund, P.E. Hopkins, Analysis of low signal-to-noise atomic resolution spectroscopy of radiation-induced Sublattice disorder in Ferritic Superalloys, Microsc. Microanal. 30 (2024) ozae044.655, https://doi.org/10.1093/mam/ozae044.655.
[43] G. Kresse, J. Furthmüller, Efficient iterative schemes for ab initio total-energy calculations using a plane-wave basis set, Phys. Rev. B 54 (1996) 11169–11186, https://doi.org/10.1103/PhysRevB.54.11169.
[44] G. Kresse, J. Furthmüller, Efficiency of ab-initio total energy calculations for metals and semiconductors using a plane-wave basis set, Comput. Mater. Sci. 6 (1996) 15–50.
[45] J. Perdew, J.A. Chevary, V. H, K. Jackson, M. Pederson, D. Singh, C. Fiolhais, Atoms, molecules, solids, and surfaces: applications of the generalized gradient approximation for exchange and correlation, Phys. Rev., B Condens. Matter 46 (1992) 6671–6687, https://doi.org/10.1103/PhysRevB.46.6671.
[46] P.E. Blöchl, Projector augmented-wave method, Phys. Rev. B 50 (1994) 17953.
[47] J.P. Perdew, K. Burke, M. Ernzerhof, Generalized gradient approximation made simple, Phys. Rev. Lett. 77 (1996) 3865–3868, https://doi.org/10.1103/PhysRevLett.77.3865.
[48] J. Zhang, S. Ma, Y. Xiong, B. Xu, S. Zhao, Elemental partitions and deformation mechanisms of L12-type multicomponent intermetallics, Acta Mater. 219 (2021) 117238.
[49] G. Song, Z. Sun, J.D. Poplawsky, Y. Gao, P.K. Liaw, Microstructural evolution of single Ni2TiAl or hierarchical NiAl/Ni2TiAl precipitates in Fe-Ni-Al-Cr-Ti ferritic alloys during thermal treatment for elevated-temperature applications, Acta Mater. 127 (2017) 1–16, https://doi.org/10.1016/j.actamat.2017.01.011.
[50] A.D. Brailsford, L.K. Mansur, The effect of precipitate-matrix interface sinks on the growth of voids in the matrix, J. Nucl. Mater. 104 (1981) 1403–1408, https://doi.org/10.1016/0022-3115(82)90796-6.
[51] R. Yang, Q. Zhang, P. Xiao, J. Wang, Y. Bai, Two opposite size effects of hardness at real nano-scale and their distinct origins, Sci. Rep. 7 (2017) 16053, https://doi.org/10.1038/s41598-017-14734-w.
[52] W.D. Nix, H. Gao, Indentation size effects in crystalline materials: a law for strain gradient plasticity, J. Mech. Phys. Solids 46 (1998) 411–425.
[53] Y. Takayama, R. Kasada, Y. Sakamoto, K. Yabuuchi, A. Kimura, M. Ando, D. Hamaguchi, H. Tanigawa, Nanoindentation hardness and its extrapolation to bulk-equivalent hardness of F82H steels after single-and dual-ion beam irradiation, J. Nucl. Mater. 442 (2013) S23–S27.
[54] S.J. Zinkle, A. Möslang, T. Muroga, H. Tanigawa, Multimodal options for materials research to advance the basis for fusion energy in the ITER era, Nucl. Fusion 53 (2013) 104024.
[55] J. Henry, X. Averty, A. Alamo, Tensile and impact properties of 9Cr tempered martensitic steels and ODS-FeCr alloys irradiated in a fast reactor at 325°C up to 78dpa, J. Nucl. Mater. 417 (2011) 99–103, https://doi.org/10.1016/j.jnucmat.2010.12.203.
[56] D. Mcclintock, M.A. Sokolov, D. Hoelzer, R. Nanstad, Mechanical properties of irradiated ODS-EUROFER and nanocluster strengthened 14YWT, J. Nucl. Mater. 392 (2009) 353–359, https://doi.org/10.1016/j.jnucmat.2009.03.024.
[57] D. Krumwiede, T. Yamamoto, T.A. Saleh, S.A. Maloy, G. Odette, P. Hosemann, Direct comparison of nanoindentation and tensile test results on reactor-irradiated materials, J. Nucl. Mater. 504 (2018) 135–143.
[58] M.L. Jenkins, Characterisation of radiation-damage microstructures by TEM, J. Nucl. Mater. 216 (1994) 124–156, https://doi.org/10.1016/0022-3115(94)90010-8.
[59] P.A. Ferreirós, P.R. Alonso, G.H. Rubiolo, Coarsening process and precipitation hardening in Fe2AlV-strengthened ferritic Fe76Al12V12 alloy, Mater. Sci. Eng.: A 684 (2017) 394–405.
[60] P.A. Ferreirós, P. Alonso, G.H. Rubiolo, Effect of Ti additions on phase transitions, lattice misfit, coarsening, and hardening mechanisms in a Fe2AlV-strengthened ferritic alloy, J. Alloys Compd. 806 (2019) 683–697.
[61] G. Song, Z. Sun, L. Li, B. Clausen, S.Y. Zhang, Y. Gao, P.K. Liaw, High temperature deformation mechanism in hierarchical and single precipitate strengthened ferritic alloys by in situ neutron diffraction studies, Sci. Rep. 7 (2017) 1–14.
[62] K. Ma, T. Blackburn, J.P. Magnussen, M. Kerbstadt, P.A. Ferreirós, T. Pinomaa, C. Hofer, D.G. Hopkinson, S.J. Day, P.A. Bagot, M. Moody, M.C. Galetz, A. J. Knowles, Chromium-based bcc-superalloys strengthened by iron supplements, Acta Mater. 257 (2023) 119183, https://doi.org/10.1016/j.actamat.2023.119183.
[63] T. Hong, A.J. Freeman, Effect of antiphase boundaries on the electronic structure and bonding character of intermetallic systems: NiAl, Phys. Rev. B 43 (1991) 6446–6458, https://doi.org/10.1103/PhysRevB.43.6446.
[64] H. Brager, F. Garner, G. Guthrie, The effect of stress on the microstructure of neutron irradiated type 316 stainless steel, J. Nucl. Mater. 66 (1977) 301–321.
[65] J.R. Matthews, M.W. Finnis, Irradiation creep models — an overview, J. Nucl. Mater. 159 (1988) 257–285, https://doi.org/10.1016/0022-3115(88)90097-9.
[66] D. Da Fonseca, F. Mompiou, T. Jourdan, J.-P. Crocombette, A. Chartier, F. Onimus, Evidence of dislocation loop preferential nucleation in irradiated aluminum under stress, Scr. Mater. 233 (2023) 115510.
[67] M. He, Y. Yang, F. Gao, Y. Fan, Stress sensitivity origin of extended defects production under coupled irradiation and mechanical loading, Acta Mater. 248 (2023) 118758, https://doi.org/10.1016/j.actamat.2023.118758.
[68] M.I. Brand, E.G. Obbard, P.A. Burr, Spatial distribution of primary radiation damage in microstructures, Npj. Mater. Degrad. 7 (2023) 23, https://doi.org/10.1038/s41529-023-00337-6.
[69] A.T. Motta, Amorphization of intermetallic compounds under irradiation—a review, J. Nucl. Mater. 244 (1997) 227–250.
[70] G. Martin, Phase stability under irradiation: ballistic effects, Phys. Rev. B 30 (1984) 1424.
[71] S. Doriot, F. Onimus, D. Gilbon, J.-P. Mardon, F. Bourlier, Transmission electron microscopy study of second phase particles irradiated by 2 MeV protons at 350°C in Zr alloys, J. Nucl. Mater. 494 (2017) 398–410, https://doi.org/10.1016/j.jnucmat.2017.07.020.
[72] S. Kano, H. Yang, J. McGrady, D. Hamaguchi, M. Ando, H. Tanigawa, H. Abe, Study of radiation-induced amorphization of M23C6 in RAFM steels under iron irradiations, J. Nucl. Mater. 533 (2020) 152088, https://doi.org/10.1016/j.jnucmat.2020.152088.
[73] Y. Li, G. Ran, K. Pei, X. Huang, R. Zhang, Q. Wang, B. Niu, In-situ TEM study on composition change and amorphous transformation of Laves phase precipitates in FeCrAl alloy during Fe+ irradiation, J. Nucl. Mater. 563 (2022) 153620, https://doi.org/10.1016/j.jnucmat.2022.153620.
[74] J. Bowman, P. Wang, G.S. Was, M. Bachhav, A.T. Motta, Ion irradiation induced amorphization of precipitates in Zircaloy, J. Nucl. Mater. 571 (2022) 153988, https://doi.org/10.1016/j.jnucmat.2022.153988.
[75] T.S. Byun, K. Farrell, Tensile properties of Inconel 718 after low temperature neutron irradiation, J. Nucl. Mater. 318 (2003) 292–299, https://doi.org/10.1016/S0022-3115(03)00006-0.
[76] S.E. Zeltmann, A. Müller, K.C. Bustillo, B. Savitzky, L. Hughes, A.M. Minor, C. Ophus, Patterned probes for high precision 4D-STEM bragg measurements, Ultramicroscopy. 209 (2020) 112890, https://doi.org/10.1016/j.ultramic.2019.112890.
[77] J.A. Mayer, T.M. Pollock, K.V. Vamsi, R. Seshadri, Antiphase boundaries in B2 intermetallics: proximate structures, formation energies, and chemical stability, Phys. Rev. Mater. 8 (2024) 013610, https://doi.org/10.1103/PhysRevMaterials.8.013610.
[78] Y. Li, W. Qiang, Compositional effects on the antiphase boundary energies in B2-type NiTi and NiTi-based high-entropy intermetallics, Mater. Chem. Phys. 311 (2024) 128549, https://doi.org/10.1016/j.matchemphys.2023.128549.
[79] W.Y. Wang, F. Xue, Y. Zhang, S.-L. Shang, Y. Wang, K.A. Darling, L.J. Kecskes, J. Li, X. Hui, Q. Feng, Z.-K. Liu, Atomic and electronic basis for solutes strengthened (010) anti-phase boundary of L12 Co3(Al, TM): a comprehensive first-principles study, Acta Mater. 145 (2018) 30–40, https://doi.org/10.1016/j.actamat.2017.10.041.
[80] P. Song, D. Morrall, Z. Zhang, K. Yabuuchi, A. Kimura, Radiation response of ODS ferritic steels with different oxide particles under ion-irradiation at 550 °C, J. Nucl. Mater. 502 (2018) 76–85, https://doi.org/10.1016/j.jnucmat.2018.02.007.
[81] A.E.M. Tamidi, Y. Sasajima, A. Iwase, Crystal structure analysis of irradiated Ni3Al using molecular dynamics simulation, Mater. Trans. 61 (2020) 72–77, https://doi.org/10.2320/matertrans.MT-M2019241.
[82] R. Kainuma, K. Urushiyama, K. Ishikawa, C.C. Jia, I. Ohnuma, K. Ishida, Ordering and phase separation in b.c.c. aluminides of the Ni–Fe–Al–Ti system, Mater. Sci. Eng.: A 239–240 (1997) 235–244, https://doi.org/10.1016/S0921-5093(97)00587-X.
[83] E. Schulson, The ordering and disordering of solid solutions under irradiation, J. Nucl. Mater. 83 (1979) 239–264.
[84] J. Brinkman, C. Dixon, C. Meechan, Interstitial and vacancy migration in Cu3Au and copper, Acta Metallurgica 2 (1954) 38–48.
[85] R. Dugdale, L. V, Some properties of vacancies and interstitials in Cu3Au, Philos. Mag. 1 (1956) 537–559.
[86] M. Koczak, H. Herman, A. Damask, The production and annealing of point defects in β-CuZn, Acta Metallurgica 19 (1971) 303–310.
[87] X. Chen, S. Peng, Y. Liu, S. Bai, L. Zhang, S. He, O.I. Gorbatov, X. Qu, Ductility deterioration induced by L21 phase in ferritic alloy through Ti addition, J. Mater. Res. Technol. 25 (2023) 3273–3284, https://doi.org/10.1016/j.jmrt.2023.06.176.